



## 2D-COFs-derived heteroatom-doped carbon nanosheets as high-efficiency all-solid frustrated lewis pair metal-free hydrogenation catalyst

Yang Liu<sup>a</sup>, Dong Han<sup>a</sup>, Fang Hao<sup>a</sup>, Wei Xiong<sup>a,\*</sup>, Pingle Liu<sup>a,b,c,\*\*\*</sup>

<sup>a</sup> College of Chemical Engineering, Xiangtan University, Xiangtan 411105, China

<sup>b</sup> National & Local United Engineering Research Centre for Chemical Process Simulation and Intensification, Xiangtan University, China

<sup>c</sup> Engineering Research Centre for Chemical Process Simulation and Optimization, Ministry of Education, Xiangtan University, China



### ARTICLE INFO

#### Keywords:

Metal-free hydrogenation catalysts  
2D-COFs  
B/N co-doped carbon nanosheets  
All-solid Frustrated Lewis Pair  
B-N synergism

### ABSTRACT

Metal-free catalysts without metal active sites participating in the reactions have obtained growing attraction under the drive of the economic and environmental problems. Here, 2D-COFs-driven B/N co-doped carbon nanosheets as metal-free catalyst was synthesized by Schiff-based coupling reaction and self-templated carbonization. It shows excellent catalytic performance in nitro compound hydrogenation reaction as all-solid FLP catalyst in H<sub>2</sub> system (100 % conversion of nitrobenzene and 99.89 % selectivity to aniline) without any metal active species in the catalyst. This result is the most promising compared to the previous literatures. In the study, the high crystallinity of precursor 2D-COFs is imperative for catalytic stability, and the function of B atoms modification and the B-N synergism were investigated carefully. The formation of B-N bond as a fixed all-solid FLP active center was verified, and it also indicates that B atoms introduction can make the carbon nanosheets orderly and enhance the strength and amount of the acid and base sites. The catalytic mechanism of hydrogen activation was also studied by combining the characterization results and density functional theory (DFT) calculations. The results show that the B atoms doping and defects formation efficiently accelerate the charges aggregation between B-N bonds to form Lewis pairs, and the TS searching calculations shows the significant decrease of H<sub>2</sub> dissociation barrier energy and the reaction energy, demonstrating the effectiveness of N and B co-doping strategy. This work is very promising and the metal-free catalyst is the potential alternative to traditional metal catalysts.

### 1. Introduction

In general, metal catalysts are the preferred choice in catalytic hydrogenation processes. Among them, noble metal catalysts (e.g. Pd, Ru, Pt) have superior catalytic activity under mild conditions [1,2]. And most of non-noble metal catalysts (e.g. Zr, Ni, Co) exhibit excellent catalytic properties by establishing the synergy between bi-metals as active sites [3,4]. However, the metal catalysts still face many drawbacks in any case, e.g. easy deactivation, high cost and serious pollution for the product and environment from metal leaching [5]. To fit the concept of green chemical engineering and highly effective hydrogenation, metal-free catalysts have been considered to be one of the most promising candidate materials in the catalytic hydrogenation processes. Compared with metal catalysts, metal-free catalysts do not rely on the metal particles as the active centers, which can potentially avoid the

metal pollution and the highly cost problems [6].

Carbon materials are the most popular candidates for developing metal-free catalysts thanks to their abundant reserves and chemical stability. However, lacking of functional groups and active sites makes it inert and difficult to be directly used as metal-free catalyst. Usually, heteroatoms doping is an efficient and convenient method to weaken chemical inert and improve catalytic ability of carbon materials. Heteroatoms doping (e.g. N, B, O, F) can disrupt intrinsic carbon skeleton structure and redistribute the charge of the carbon atoms and heteroatoms, which is often considered to be the potential active centers in hydrogenation reaction. For instance, Xiong et al. [7] proposed the pyrrolic-N doping and the surrounding defects construction in carbon nanotubes were the active centers for H<sub>2</sub> activation in aromatic nitro-compounds hydrogenation. Wu et al. [8] developed the N doped graphite quantum dots (GQD) for CO<sub>2</sub> hydrogenation, and found that

\* Corresponding author.

\*\* Corresponding author at: College of Chemical Engineering, Xiangtan University, Xiangtan 411105, China.

E-mail addresses: [happy.xiongw@163.com](mailto:happy.xiongw@163.com) (W. Xiong), [liupingle@xtu.edu.cn](mailto:liupingle@xtu.edu.cn) (P. Liu).

pyridinic-N species and the accompanying defects density at the edge of GQD affected the conversion of  $\text{CO}_2$  and the selectivity to  $\text{CH}_4$ . Meanwhile, the heteroatoms multi-doping strategy has also been developed, and it is easier to produce the special interaction and new catalytic active sites among heteroatoms [9]. Gao et al. [10] prepared P atoms and N atoms co-doped cellulose (PNC) for nitroarenes hydrogenation. In their work, PNC catalyst had relative smaller electronic resistance and P/N dopants could regulate the charge distributions and lead to an impurity energy level near fermi level, which was beneficial to nitroarenes hydrogenation. Nonetheless, the role of heteroatoms, the exact active centers and the catalytic mechanism have not been fully clarified. In addition, the choice of hydrogen source is equally important in the process of catalytic hydrogenation. Commonly hydrogen donors roughly include isopropanol [11],  $\text{NaBH}_4$  [12],  $\text{N}_2\text{H}_2\text{-H}_2\text{O}$  [13] and  $\text{H}_2$  [14]. In general, the organic hydrogen donors are often corrosive, high cost and some may be toxic [15,16]. In contrast,  $\text{H}_2$  is more suitable for environment-friendly industrial hydrogenation process due to its economic and clean advantages [17]. However, the development of metal-free catalysts is extremely challenging in  $\text{H}_2$  hydrogenation system. Therefore, it is necessary to develop an efficient and utility metal-free catalyst with  $\text{H}_2$  as hydrogen donor to further explore the reaction mechanism and activity source.

In recent years, the Frustrated Lewis Pair (FLP) concept has been developed as a metal-free catalyst to provide potential reactivity for activating small molecules. Stephan [18] first proposed FLP theory by synthesizing compounds  $(\text{Mes})_2\text{PC}_6\text{F}_4\text{B}(\text{C}_6\text{F}_5)_2$ , among which B atom as Lewis acid and P atom as Lewis base, as sterically frustrated Lewis acid and Lewis base to active  $\text{H}_2$  molecules, and synergistically promoted the protonation of the base and hydride at the Lewis acid. Henceforth, the theory of FLP has been applied to heterogeneous catalytic hydrogenation systems [19,20]. Among them, the development of metal-free catalyst was more about assembling heteroatoms as Lewis acids and Lewis bases into rigid structures to form FLP catalyst to improve the stability of catalysts and reactivity to  $\text{H}_2$  molecules. In fact, the construction of FLP catalyst with rigid structure as a precursor can not only maintain the chemical stability of the catalyst but also enhance the adsorption capacity and mass transfer kinetics performance of the catalyst by chemical modification [21]. And the required of no-bonding is not necessary. The FLP reactivity can be showed in the system at equilibrium that provides dissociated Lewis acid and base, thus the FLP catalyst that has not sufficient steric and electronic frustration can also react with  $\text{H}_2$  and other substrate molecules [22,23]. Zhang et al. [24] created a series of FLPs with different acid-base distance on  $\text{ZnSn}(\text{OH})_6$  cube to capture and active  $\text{CO}_2$  molecule. The results show that smaller FLP distance (0.207 nm) on (111) facet exhibits stronger capturing ability of  $\text{CO}_2$  than that on (100) facet (0.488 nm), the typical distance between  $\text{O}_{\text{vs}}$  (oxygen vacancy) Lewis acid and Zn-OH Lewis bases. Based on the study, Su et al. [25] successfully designed an all-solid FLP catalyst of B, N co-doped nanodiamond by using precursors of nanodiamond and ionic liquids containing N and B atoms. It is believed that the B atoms and N atoms in the material were bonded to form an unquenched Lewis pair to decompose hydrogen to form active  $\text{H}^+/\text{H}^-$ , and realized the hydrogenation reaction of the substrate. This study provides significant fundament for the design and modification of metal-free FLP catalysts, which are very attractive since no metal species participating in the reaction. The inspiration of this present work was based on these advanced fundamental researches. However, the practical construction and application of all-solid FLP metal-free catalysts still face several problems, such as low catalytic efficiency, complex design, and high cost. Therefore, developing an alternative high-efficiency and low-cost all-solid FLP metal-free catalysts by facile preparation method has become the pressing needs.

The two-dimension covalent organic frameworks (2D-COFs) is a popular new porous polymer with stability of geometry structure and excellent designability [26]. And its derived carbon materials, remained the rigid skeleton morphology and the inherent heteroatoms property of

2D-COFs to a large extent, are excellent candidates for designing the all-solid FLP metal-free catalysts [27,28]. In this work, all-solid FLP metal-free catalysts of B/N co-doped carbon nanosheets were prepared by self-template carbonization with doping  $\text{B}_2\text{O}_3$  on 2D-COFs. And the nitrobenzene hydrogenation was chosen as probe reaction to investigate the catalytic performances. The reaction results show that the crystallinity of both of 2D-COFs (COF-MP and COF-UB) have an influence on the hydrogenation process, and the metal-free MP-BNC and UB-BNC catalysts exhibit excellent catalytic properties after B atoms modification. Then the function of B atoms modification and the catalytic mechanism were investigated systematically by combining catalytic characterization and DFT calculations. The analysis results indicate that the synergistical effects of B-N Lewis pairs and defects could alter the inertness of carbon materials and activate the  $\text{H}_2$ , hence immensely improve the hydrogenation properties. This metal-free B/N co-doped carbon nanosheets is very promising as all-solid FLP metal-free catalyst in hydrogenation reaction under  $\text{H}_2$  system, and it is also the potential alternative to traditional metal catalysts.

## 2. Experimental

### 2.1. Catalysts preparation procedures

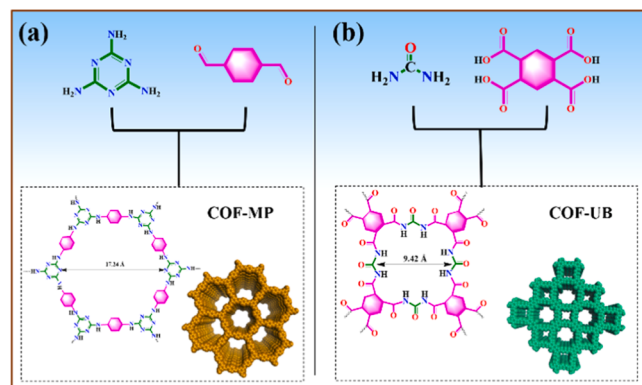
#### 2.1.1. Synthesis of two different 2D-COFs materials (COF-MP and COF-UB)

The specific preparation process of COF-MP was as follows: 18 mmol terephthalaldehyde and 12 mmol melamine were added to a 250 ml round-bottomed flask containing 100 ml ethanol, ultrasound until dissolved. Then, the mixture was stirred for 1 h at room temperature, sequentially heated to 105 °C for 48 h, finally cooled to room temperature. The product was filtered and separated, washed with deionized water and ethanol for several times, and then dried overnight in a vacuum oven at 70 °C for 12 h to obtain COF-MP.

COF-UB was prepared as follows: 10 mmol pyromellitic acid and 5 mmol  $\text{NH}_4\text{Cl}$  were added to a 250 ml round-bottomed flask containing 100 ml ethanol, ultrasound until dissolved. Then, heated to 100 °C for 3 h and sequentially added 40 mmol urea until dissolved, finally dried under 200 °C and hold 3 h to obtain COF-UB. The preparation processes of the two 2D-COFs precursors are shown in **Scheme 1**.

#### 2.1.2. MP-BNC and UB-BNC preparation

Boron modification of the original 2D-COFs was synthesized by the hot immersion stirring method. Firstly, 2 g  $\text{B}_2\text{O}_3$  was dissolved in 50 ml ethanol for 30 min under stirring, then 2 g as-prepared 2D-COFs was added. The mixture was ultrasound for 30 min, stirred at room temperature for 3 h and then heated to 90 °C for 6 h. The mixture was dried at 80 °C in the oven overnight to get B modified 2D-COFs. The obtained materials were thermally treated for 2 h in a tube furnace at a heating



**Scheme 1.** The preparation diagram of two 2D-COFs precursors of COF-MP (a) and COF-UB (b).

rate of  $2^{\circ}\text{C}\cdot\text{min}^{-1}$  under  $\text{N}_2$  atmosphere. The calcination temperature was controlled at  $800^{\circ}\text{C}$ . After cooling to room temperature, the residual  $\text{B}_2\text{O}_3$  was removed by washing with boiling water. Then the materials were filtrated and dried at  $80^{\circ}\text{C}$  overnight and named as MP-BNC or UB-BNC.

### 2.1.3. MP-NC and UB-NC preparation

In order to investigate the function of B atoms modification, the contrastive samples of MP-NC and UB-NC without B modification was obtained by directly thermally treatment of 2D-COFs under  $800^{\circ}\text{C}$  for 2 h in a tube furnace under  $\text{N}_2$  atmosphere.

### 2.2. Catalytic test procedure

Nitrobenzene hydrogenation was carried out in a 50 ml Teflon-lined stainless steel autoclave. Firstly, the reactants, solvent ethanol and catalyst were placed in the autoclave, then the reactor was flushed with  $\text{N}_2$  and  $\text{H}_2$  in turn for several times. Finally, the reaction continued by adjusting the reaction temperature, the stirring speed,  $\text{H}_2$  pressure and the reaction time. After the reaction, the reactor was cooled to room temperature and preserving reaction solution.

The products were separated and analyzed by the high-performance liquid chromatography (HPLC) equipped with the UV detector (SPD-20A) and column (Agilent ZORBAX SB-C18, 5  $\mu\text{m}$ , 4.6  $\times$  250 mm). And the detection wavelength was 254 nm, and the elution liquid ratio was methanol: water = 40:60 (volume fraction) with a flow rate of 1.0  $\text{ml}/\text{min}$ .

## 3. Results and discussions

### 3.1. Characterization and catalytic performance of MP-NC and MP-BNC derived from COF-MP

XRD spectra of original COF-MP is shown in Fig. 1a, the

characteristic peaks exist at  $1.56^{\circ}$ ,  $17.6^{\circ}$ ,  $21.6^{\circ}$ ,  $26.1^{\circ}$ ,  $27.0^{\circ}$ ,  $28.7^{\circ}$ ,  $29.6^{\circ}$ . In particular, the peak at  $2\theta = 17.6^{\circ}$  belongs to the diffraction peak of the repeated structural unit formed by the superposition of successive triazine rings in the plane, and  $2\theta = 27^{\circ}$  ascribes to the (002) plane of the structural aromatic ring unit filled in the interlayer, indicating that the prepared COF-MP has certain crystallinity [29]. TG curve of COF-MP in Fig. 1b shows that it experiences slight weight loss by evaporating surface moisture and solvent before  $125^{\circ}\text{C}$ , and the most serious weight loss between  $125^{\circ}\text{C}$  and  $574.5^{\circ}\text{C}$  are the losing of residual organic monomers (e.g. melamine deamination and terephthaldehyde sublimation) and the peeling of some oxygen-containing functional groups in the structure of COF-MP, until it turns into stable weight at  $800^{\circ}\text{C}$ .

FT-IR spectra in Fig. 1c also shows that the COF-MP materials was successfully synthesized, and the characteristic bands of  $-\text{NH}_2$  stretching are located at  $3417.8\text{ cm}^{-1}$  and  $3468.9\text{ cm}^{-1}$ , a set of intense band at  $1580\text{ cm}^{-1}$  belongs to the imine ( $\text{Ar}-\text{C}=\text{N}$ ) stretching vibration and the peak at  $1150\text{ cm}^{-1}$  is related to the C-N stretching of  $-\text{NH}-$  [30]. After high-temperature carbonization of COF-MP and B-COF-MP, the characteristic bands of COF-MP disappear. While a broad and strong band at  $1600\text{ cm}^{-1}$  which is assigned to C-C stretching in carbon materials (MP-NC and MP-BNC) appears. In MP-BNC catalyst, the B-N bond appears at both  $798\text{ cm}^{-1}$  and  $1372\text{ cm}^{-1}$ , and the characteristic peak of C-B band is located at  $1000\text{ cm}^{-1}$  [31], indicating that B atoms are successfully doped into the COF-MP structure after B atoms introduction and carbonization.

The  $\text{N}_2$  adsorption-desorption isotherms of COF-MP, MP-NC and MP-BNC are shown in Fig. 1d, MP-BNC exhibits obvious mesoporous structure, with larger average pore diameter around  $30\text{ \AA}^{-1}\sim 50\text{ \AA}^{-1}$ . In Table S1, the specific surface area (SSA) of MP-NC ( $336.2\text{ m}^2\cdot\text{g}^{-1}$ ) is lower than original COF-MP ( $547.76\text{ m}^2\cdot\text{g}^{-1}$ ), resulting from the contractile pore and the stacked carbon nanosheets after carbonization. However, MP-BNC shows larger SSA of  $408.95\text{ m}^2\cdot\text{g}^{-1}$  by post introduction of B atoms, which may due to the volatilization of boron

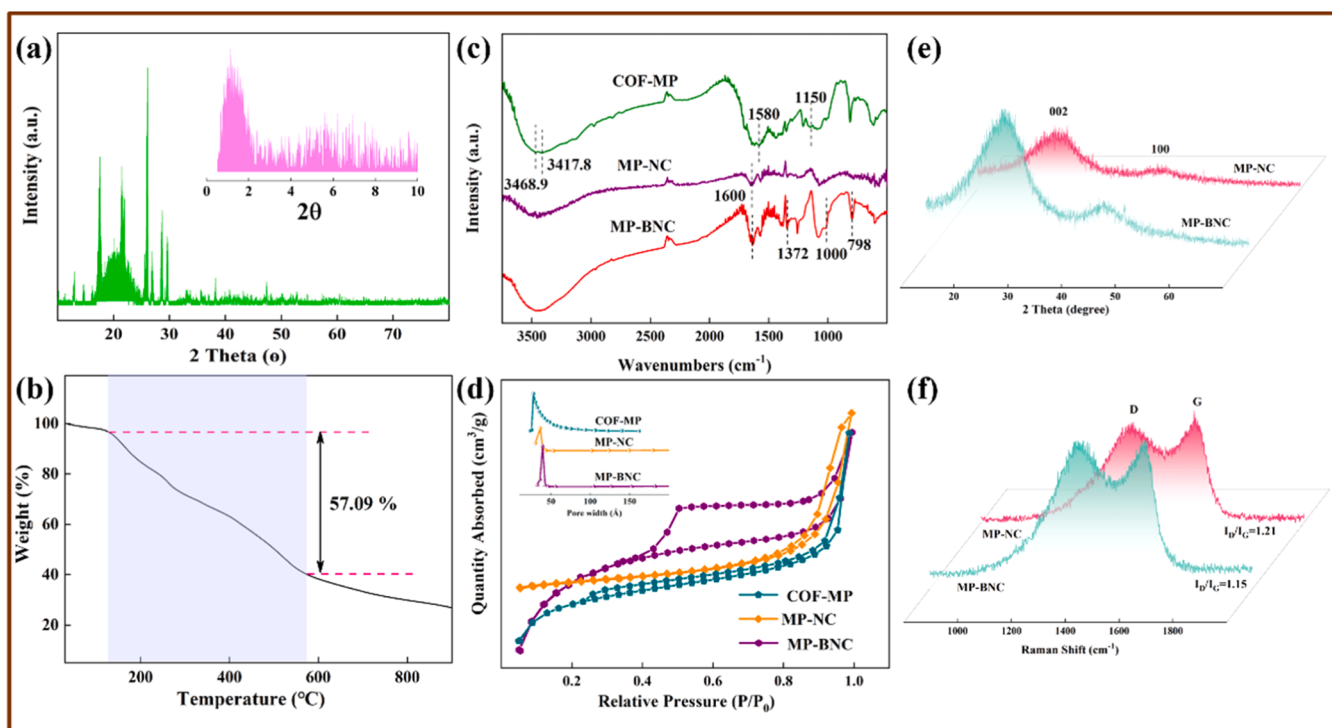


**Fig. 1.** XRD spectra (a), TG curves of COF-MP precursor (b), FT-IR spectra of COF-MP, MP-NC (derived directly from COF-MP) and MP-BNC (derived from B modified COF-MP) (c),  $\text{N}_2$  adsorption-desorption isotherms and pore width distributions of COF-MP, MP-NC and MP-BNC (d), XRD spectra (e) and Raman spectra (f) of MP-NC and MP-BNC<sup>1</sup>. <sup>1</sup>COF-MP is the original 2D-COF material before pyrolysis; the MP-NC sample was derived directly from COF-MP without boron modification, while the MP-BNC was derived from B modified COF-MP. These abbreviations also apply to the following discussion content.

precursor (melting point 450 °C) during calcination by forming large numbers of mesopores. And larger SSA and pore size are conducive to the diffusion and mass transfer of reactant molecules. These results show that the originally densely packed structure of COF-MP gradually becomes loose and porous, providing the adequate environment for H<sub>2</sub> molecules and reactants interacting with active sites.

Commonly, the structure of precursor affects the formation and arrangement of carbon layers. In Fig. 1e of the XRD diffraction, the broad peaks located at 20 = 25° and 43.3° are the (002) and (100) planes of graphite carbon, indicating a typical sp<sup>2</sup> amorphous carbon structure of MP-NC and MP-BNC. More obviously, the peak intensities of (002) and (100) planes in MP-BNC are sharper than those in MP-NC, showing that some defects may be removed and the amorphous carbon gradually turned into an orderly graphite structure after introducing B atoms, and formed long-range-ordered graphite layers [32].

For carbon materials, controlling the defect degree is beneficial to increasing the pores utilization and maintaining structural stability. From Raman spectra in Fig. 1f, the stretching of the C-C bond in graphitic material produces G band at 1592 cm<sup>-1</sup>, and the existence of disorder leads to the appearance of D band at 1335 cm<sup>-1</sup>, which is common to sp<sup>2</sup> carbon systems in resonance Raman spectra. Disorder quantification in carbon materials is achieved by analyzing the I<sub>D</sub>/I<sub>G</sub> ratio [33]. The I<sub>D</sub>/I<sub>G</sub> value of MP-NC is 1.21, while the I<sub>D</sub>/I<sub>G</sub> value of the MP-BNC catalyst decreased to 1.15. It can be inferred that B atoms introduction may fill the inherent defects of the NC structure, reduce the distortion of the carbon lattice and the regeneration of topological defects, thus the carbon skeleton can be more chemically stable and complete in MP-BNC after B introduction [30].

SEM spectra of COF-MP (a, b, c), MP-NC (d, e, f) and MP-BNC (g, h, i) are shown in Fig. S1. Original COF-MP presents irregular particles, while

the partial size of MP-NC (after pyrolysis) decreases clearly for the shrinkage, but the skeleton morphology does not change (Fig. S1 and Fig. 2a). While the MP-BNC catalyst forms randomly arranged and stacked stratiform carbon structure (Fig. S1 and Fig. 2d) after post boron modification on the original COF-MP. In HRTEM (Fig. 2b and e), MP-NC catalyst is mostly distorted and has short carbon lattice, while MP-BNC has more obvious lattice long fringe structure around 0.35 nm, which are close to the graphene lattice. This also shows that the B atoms introduction makes the carbon nanosheets gradually orderly [34]. The AFM results (Fig. 2c, f) show that the obtained carbon nanosheets present uneven size distribution in both samples. The MP-NC has an average island width size of 98.82 nm and height of 2.11 nm. In contrast, the MP-BNC has a larger and thinner layer carbon nanosheet structure, showing an average island length of 436.46 nm and thickness of 0.81 nm. Meanwhile, it can also find that the surface of the MP-BNC is smoother than MP-NC. EDS-mapping images of MP-BNC (Fig. 2g) show that N atoms and B atoms are distributed evenly throughout the carbon nanosheets. Obviously, B atoms introduction has a substantial impact on the morphology of the carbon structure, these stacked nanosheets determine higher specific surface area of the BNCs materials, which may expose more active sites.

The XPS survey spectra of MP-NC and MP-BNC are shown in Fig. 3a, in which the peaks at around 191 eV, 284 eV, 400 eV and 530 eV describe to B1s, C1s, N1s and O1s, respectively. Table 1 shows the atom amounts and the chemical state of different elements. Compared with MP-NC, the surface N atoms content on MP-BNC decrease from 9.26 % to 4.86 % after B atoms introduction. It is known that the formation energy of B1s is lower than N1s, which makes B atoms more easily embedding into the carbon lattice than N atoms, resulting in partially losing of free N atoms during carbonization [35]. The well-fitted peaks in C1s spectra

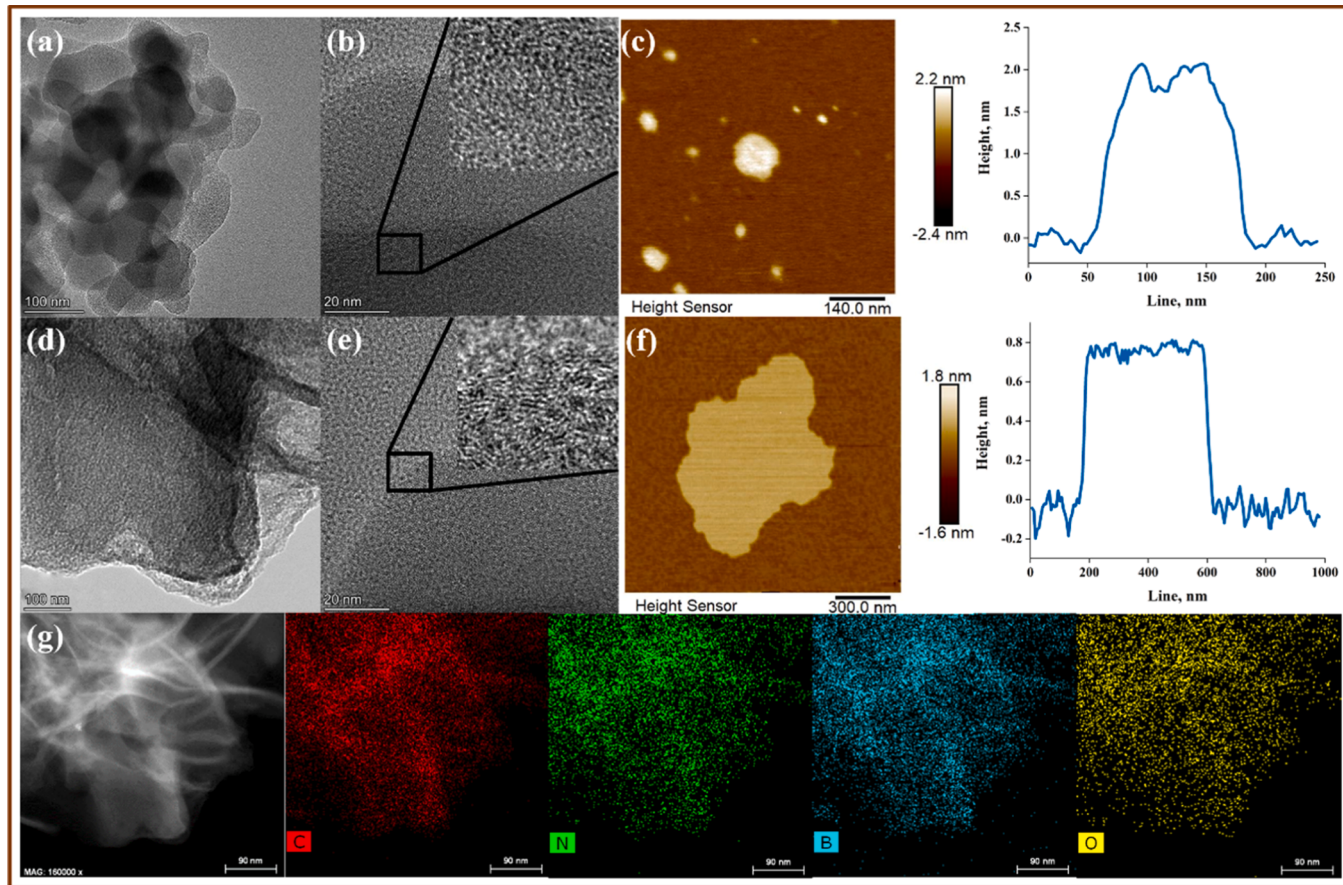
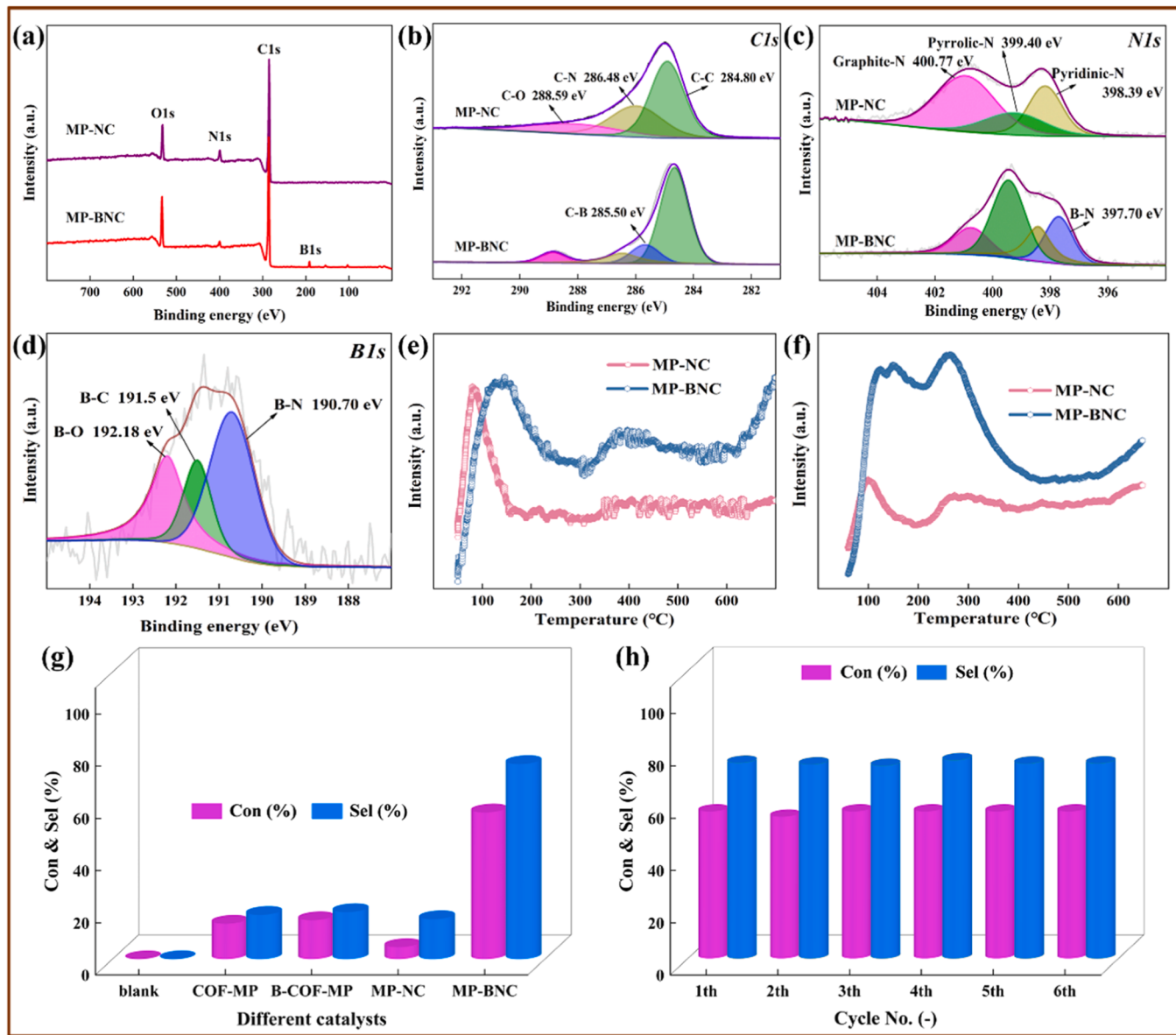


Fig. 2. TEM spectra of MP-NC (a, b) and MP-BNC (d, e), AFM images and height profiles along line of MP-NC (c) and MP-BNC (f), the corresponding EDS-mapping images of MP-BNC (g).



**Fig. 3.** XPS survey spectra (a), C1s spectra (b), N1s spectra (c) of MP-NC and MP-BNC, B1s spectra of MP-BNC (d), CO<sub>2</sub>-TPD (e) and NH<sub>3</sub>-TPD (f) of MP-NC and MP-BNC, the catalytic performance of different samples (g), and the cycling stability of MP-BNC (h)<sup>2</sup>. Reaction conditions: Nitrobenzene 0.05 g, Ethanol 20 ml, Catalyst 0.05 g, Reaction temperature 180 °C, H<sub>2</sub> pressure 4 MPa, Reaction time 18 h.

**Table 1**

The different elements amount and the proportion of different bond types in catalysts.

Samples	C (at%)	N (at%)	B (at%)					B (at%)			
			Amount	B-N	Pyridinic-N	Pyrrolic-N	Graphite-N	Amount	B-N	B-C	B-O
MP-NC	75.60	9.26	-	26.63	21.07	52.30	-	-	-	-	-
MP-BNC	76.18	4.86	22.43	19.45	42.30	15.82	5.45	51.37	29.72	22.17	

of MP-NC and MP-BNC (Fig. 3b) are assigned to C-C (284.80 eV), C-B (285.50 eV), C-N (286.48 eV) and C-O (288.59 eV), respectively [36]. Together with Table S2, the content of C-C bond increases from 50.40 % to 67.63 % in C1s spectra after B modification, indicating high degree of carbonization of the samples, which is consistent with the XRD results. However, the content of C-N bond decreases, which might due to the combining of N-B bond by interacting between partial N atoms and B atoms. The N1s and B1s spectra in Fig. 3c and d prove this hypothesis. The N1s spectra can be fitted into peaks of 397.70 eV, 398.39 eV, 399.40 eV and 400.77 eV, corresponding to the B-N, pyridinic-N,

pyrrolic-N and graphite-N, respectively. And the B1s spectra can be deconvoluted into three types of B: B-N (190.70 eV), B-C (191.50 eV) and B-O (192.18 eV) [37]. Compared with MP-NC, the contents of graphite-N and pyridinic-N in MP-BNC decrease obviously (52.30 % decreases to 15.82 % with graphite-N, 26.63–19.45 % with pyridinic-N), but the content of pyrrolic-N increases from 21.23 % to 42.30 % and the B-N bond appears (occupies 22.43 %). These results may infer that more graphite-N and slight pyridinic-N are combined with B atoms in the structure of MP-BNC. This is consistent with that B-N bond occupies dominant role in B1s spectra (accounting for 51.37 %). From the above

analysis, it indicates that the electron-deficient B atoms are easier to interact with the electron-rich N atoms, so that the active N species can be firmly embedded in the carbon lattice, leading to more stable properties of MP-BNC than MP-NC [35]. In previous reports, the N atom, as a Lewis base, had an nucleophilic behavior, and it easily formed an unstable intermediate during the hydrogenation of nitrobenzene [38,39]. After the incorporation of the B atoms, the B atom acts as a Lewis acid to form a stable B-N bond with the N atom [40]. In the work, after B introduction, the formed B-N bonds in MP-BNC catalyst are the most probable active centers for hydrogenation reaction as Frustrated Lewis Pairs, in which the embedded B and N atoms with special electronic properties could be used as weak Lewis acid and weak Lewis base sites to capture and release electrons, so that it could be great catalytic active sites for H<sub>2</sub> molecules absorption and dissociation during the hydrogenation reaction [41,42].

In order to judge the acidity and basicity of the samples and further confirm the Frustrated Lewis Pair properties, CO<sub>2</sub>-TPD and NH<sub>3</sub>-TPD were carried out for MP-NC and MP-BNC. It can be seen from the CO<sub>2</sub>-TPD curves (Fig. 3e) that there is almost no obvious peak after 150 °C in MP-NC, indicating that graphite-N has little contribution to the basicity of the catalyst due to the weak basicity of graphite-N just like the original carbon structure. After introduction of boron, the MP-BNC catalyst has a prominent peak of weak basic site between 300 °C and 450 °C, this may due to the combination of B atoms with graphite-N and leaving more pyrrolic-N and larger basicity of the catalyst. The shifting of CO<sub>2</sub> desorption peak to higher temperature in MP-BNC also indicates stronger basicity after B introduction. In NH<sub>3</sub>-TPD curves (Fig. 3f), the weak acidity of MP-NC was shown between 200 °C and 400 °C [7]. In MP-BNC, the participation of B atoms leads to higher peak intensity of NH<sub>3</sub> desorption, further indicating that doping of B atoms increases acid contents in the BNCs structure. Both of CO<sub>2</sub>-TPD and NH<sub>3</sub>-TPD results demonstrate that these metal-free hydrogenation catalysts possess both acid and basic properties, and introduction of B atoms could enhance the strength and amount of the acidity and basicity, which may originate from the B-N Lewis pairs generation.

The catalytic performance of these metal-free N doped carbon materials and B/N co-doped carbon materials are investigated by using nitrobenzene hydrogenation as probe reaction (Fig. 3g). There is no nitrobenzene conversion in the blank experiment. The original COF-MP and B-COF-MP show limited catalytic activity and they are not stable in the system as well. After carbonization at 800 °C, the MP-NC shows even poorer activity with 4.67 % conversion of nitrobenzene and 15.41 % selectivity to aniline. On the contrary, the MP-BNC catalyst exhibits catalytic performance with 56.30 % conversion of nitrobenzene and 74.84 % selectivity to aniline, which is much higher than that of MP-NC. This result is inspiring and the stability of this sample is also perfect, and the MP-BNC was filtered after reaction and applied directly in the next turn during the recycle stability investigation. The results in Fig. 3h show that MP-BNC maintain stable catalytic performance after 6 cycles, the conversion of nitrobenzene is larger than 55 % and the selectivity is stable (> 70 %). These metal-free catalysts can avoid deactivation from metal leaching or poisoning in comparison with metal hydrogenation catalysts. The calcination temperature of the catalyst is also tested, it indicates that higher or lower calcination temperature leads to different catalytic performance (in Fig. S2). MP-BNC calcined at 700 °C shows 39.48 % conversion of nitrobenzene and 67.22 % selectivity to aniline, the reason may be that insufficient carbonization causes limited B atoms and N atoms to embed into the carbon lattice and thus forming limited active sites. While the carbonization temperature of 900 °C will result in damaged structural framework of catalyst and loss of active sites, thus affect the catalytic performance. It gives only 3.8 % conversion of nitrobenzene and 5.17 % selectivity to aniline over MP-NC-900 without B atom modification. And MP-BNC-900 gives 41.68 % conversion of nitrobenzene and 64.66 % selectivity to aniline. These results can also prove that B atoms doping can improve the catalytic performance during the metal-free hydrogenation reaction.

Combing the characterization results and catalytic performance of these metal-free catalyst, it has been proved that MP-BNC has excellent physical and chemical features, especially the formed Frustrated Lewis Pair of B-N bond, which can mobilize the transfer of electrons between atoms and play a key role in H<sub>2</sub> molecules adsorption and dissociation during the hydrogenation reaction [5,39].

### 3.2. The screening of 2D-COFs precursor with high crystallinity

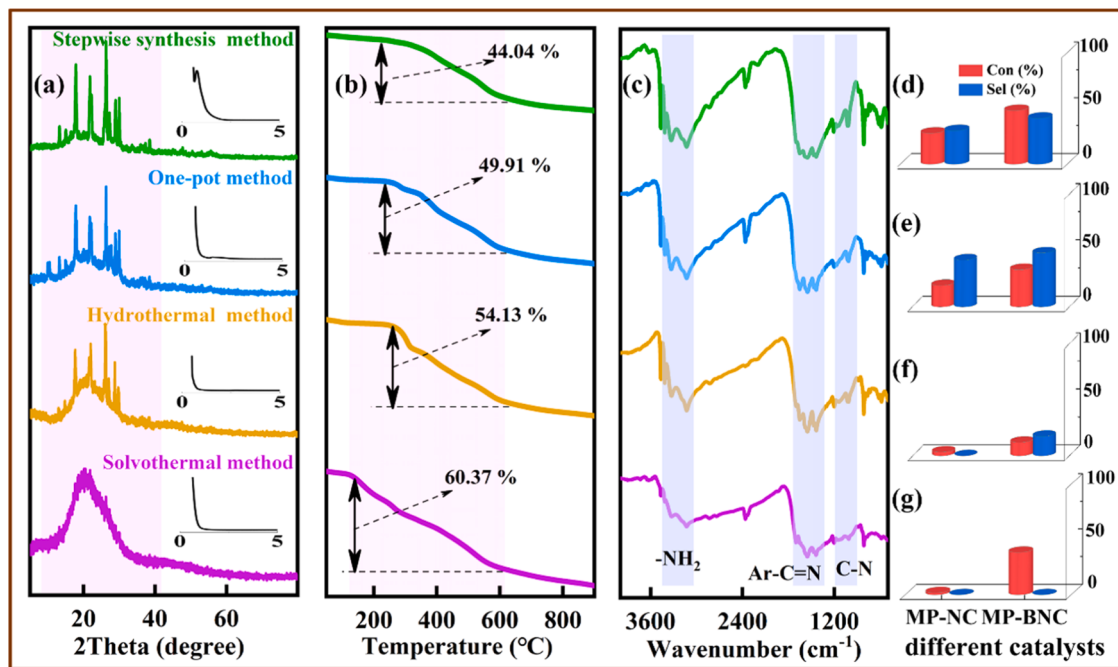
In this work, it was found that the crystallinity of COF-MP is difficult to be controlled in the preparation process, which seriously affects the reproducibility of the catalyst and interferes with the catalytic activity. Thus, it is necessary to find a suitable method to stabilize the crystallinity of COF-MP, and the following four different methods (the solvothermal method, hydrothermal method, one-pot method and stepwise synthesis method) for COF-MP preparation were studied in Fig. 4.

Fig. 4a shows the XRD spectra of COF-MPs, the diffraction peaks of COF-MP prepared by the stepwise synthesis method become sharp and strong. In addition, the weight plunges of all the samples were significant at temperature ranges of 200–600 °C due to the decomposition of organic functional groups (Fig. 4b) [43]. FT-IR spectra of COF-MPs (Fig. 4c) show the characteristic bands of -NH<sub>2</sub> stretching, imine (Ar-C=N) stretching vibration and C-N stretching of -NH- in all the samples [30]. Compared the catalytic performances of MP-NCs and MP-BNCs derived from COF-MPs via different methods, the samples prepared by stepwise synthesis method show best catalytic performance in nitrobenzene hydrogenation, MP-NC exhibits 27.73 % conversion of nitrobenzene and 30.02 % selectivity to aniline, and the MP-BNC shows 48.15 % conversion of nitrobenzene and 41.25 % selectivity to aniline after boron modification (Fig. 4d, e, f, g). Combining with the above analysis, the crystallinity of COF-MP is closely related to the catalytic performance. The high crystallinity of COF-MP obtained by stepwise synthesis method benefits to the catalytic performance of its derivatives of both MP-NC and MP-BNC.

However, the crystallinity of COF-MP under the stepwise synthesis method is still in low level due to the partially condensation reaction of melamine and terephthalaldehyde. And the crystallinity could directly influence the element contents in MP-NCs and MP-BNCs catalysts. To develop a 2D-COFs material with higher crystallinity, a new COF material was constructed by the former mentioned stepwise synthesis method with pyromellitic acid and urea as the rigid monomer. This 2D-COFs material was named as COF-UB (its preparation diagram has been shown in Scheme 1).

### 3.3. Characterization and catalytic performance of UB-NC and UB-BNC derived from COF-UB

Compared with COF-MPs, cleaner crystal peaks at 19.04°, 19.98°, 26.46°, 28.28°, 29.96°, 32.88° and a peak in the small angle region at 2.44° belong to COF-UB (Fig. 5a), indicating the successful synthesis and high crystallinity of COF-UB. In the TGA curve of Fig. 5b, the weight loss in the 200 ~ 450 °C region corresponds to the decomposition of the organic functional groups and roughly terminates at 600 °C in COF-UB structure. From XRD and XPS characterization of UB-NC-T (T represent 600–800 °C) show the graphitization and element distribution are sustainable change with the increase of calcination temperature in Fig. S3, indicating that the UB-NC-600 catalyst is only stable in weight but the graphitization and element distribution not change to the optimum state. The FT-IR spectra show the linking group imine (Ar-C=N) stretching vibration between pyromellitic acid and urea in Fig. 5c. These results prove that the structure of COF-UB is more perfect than that of COF-MP. The Fig. 5d show the catalytic performances of these different materials. COF-UB and B-COF-UB have no hydrogenation activity before pyrolysis. The UB-NC catalyst shows 60.20 % nitrobenzene conversion and 26.03 % selectivity to aniline after pyrolysis. However, after boron modification, UB-BNC catalyst gives the best performance of 100 %



**Fig. 4.** XRD survey spectra (a), TGA curve (b), FT-IR spectra (c) of COF-MPs prepared by different method. The catalytic performance of MP-NCs and MP-BNCs derived from COF-MPs via the stepwise synthesis method (d), one-pot method (e), hydrothermal method (f) and solvothermal method (g). Reaction conditions: Nitrobenzene 0.05 g, Ethanol 20 ml, Catalyst 0.05 g, Reaction temperature 180 °C, H<sub>2</sub> pressure 4 MPa, 18 h.

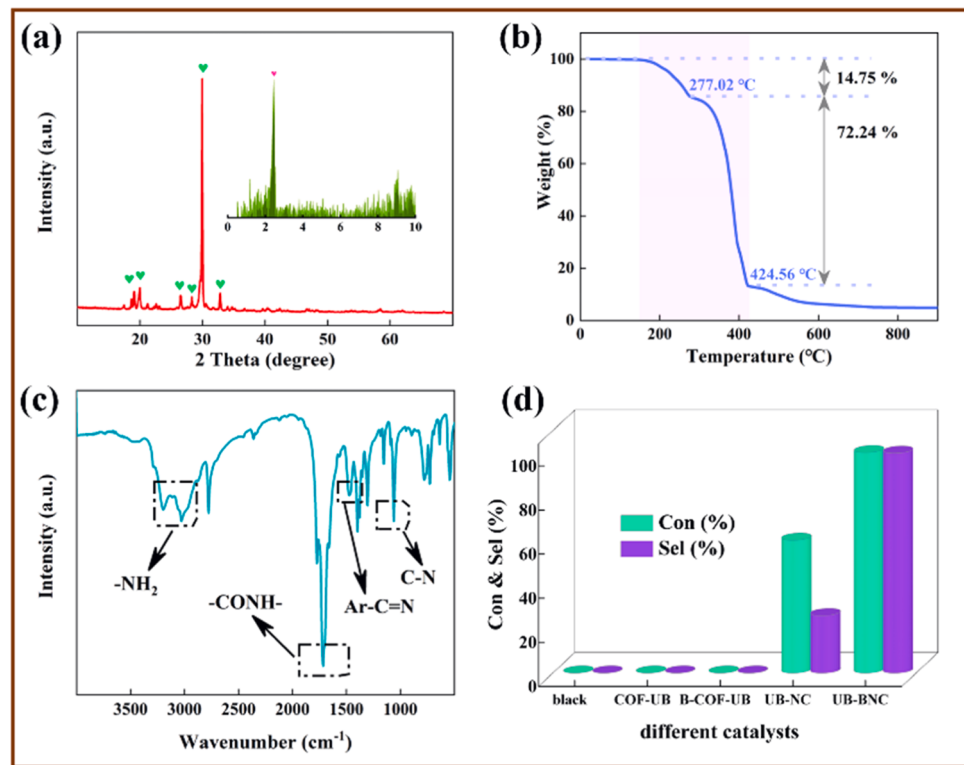


**Fig. 5.** XRD survey spectra (a), TGA curve (b), FT-IR spectra (c) of COF-UB, the catalytic performance of different catalyst from COF-UB (d). Reaction conditions: Nitrobenzene 0.05 g, Ethanol 20 ml, Catalyst 0.05 g, Reaction temperature 180 °C, H<sub>2</sub> pressure 4 MPa, 18 h.

nitrobenzene conversion and 99.89 % selectivity to aniline under optimum reaction conditions (shown in Fig. S4).

UB-NC and UB-BNC catalysts were derived from COF-UB, and their properties are shown in Fig. 6. As the TEM image of Fig. 6a, b, c, d and AFM images of Fig. 6e, f shown, the UB-NC catalyst presents short

graphene-like lattice with the size of 588 nm and height of 1.33 nm, which is close to the single graphene sheet structure. The UB-BNC (after B modification) exhibits obvious fingerprint graphite lattice with the size of 347 nm and thickness of 1.903 nm, which is more conducive to the formation of rigid network structure that can prevent shrinkage

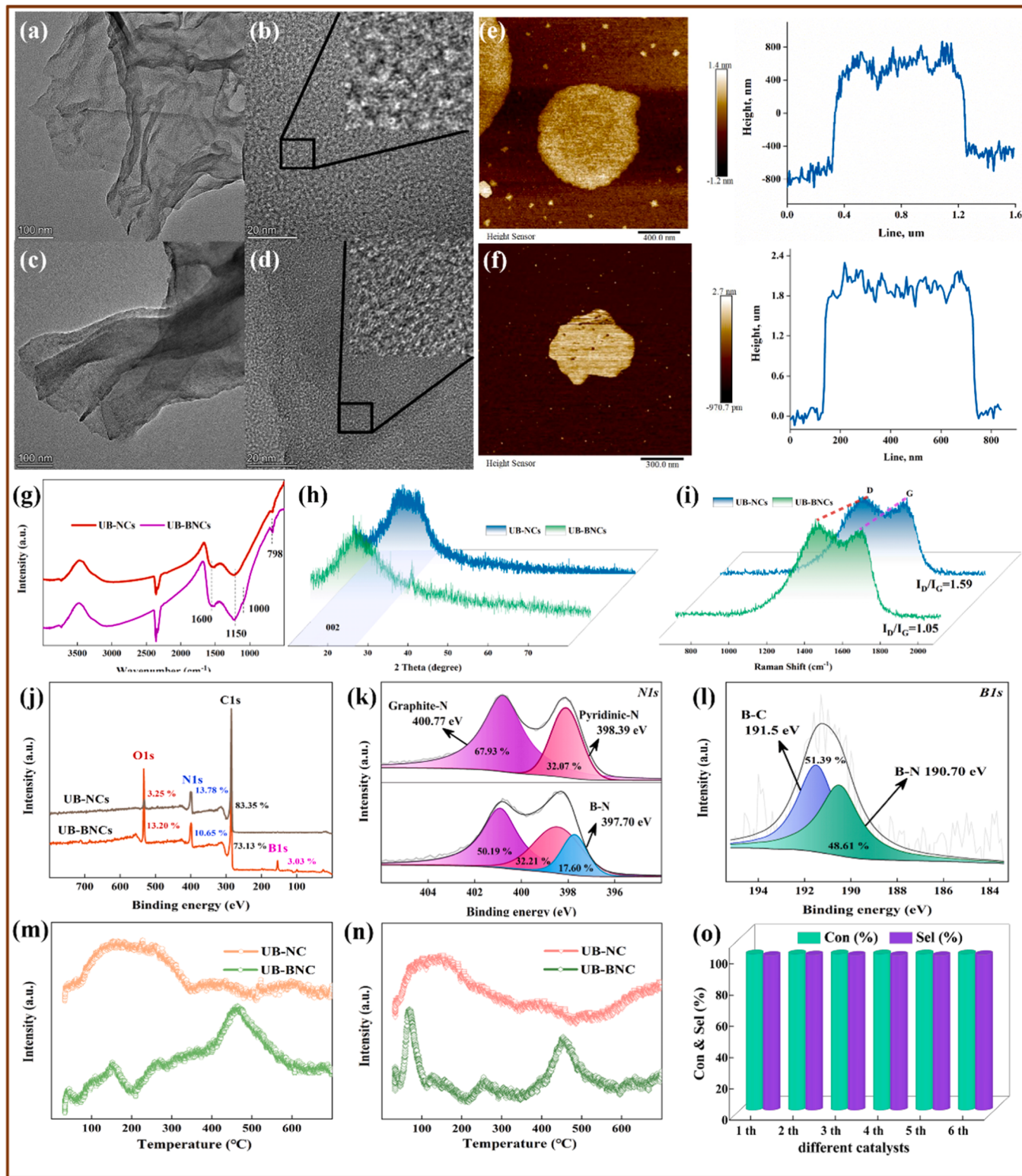


**Fig. 6.** TEM spectra of UB-NC (a, b) and UB-BNC (c, d), AFM images and height profiles along line of UB-NC (e) and UB-BNC (f), FT-IR spectra (g), XRD survey spectra (h), Raman spectra (i), XPS survey spectra (j), N1s spectra (k), B1s spectrum of UB-BNC (l), CO<sub>2</sub>-TPD (m) and NH<sub>3</sub>-TPD (n) of UB-NC and UB-BNC, the Cycling stability of UB-BNC (o). Reaction conditions: Nitrobenzene 0.05 g, Ethanol 20 ml, Catalyst 0.05 g, Reaction temperature 180 °C, H<sub>2</sub> pressure 4 MPa, 18 h.

[44]. The SSA of the catalysts are 26.91 m<sup>2</sup>·g<sup>-1</sup> and 221.41 m<sup>2</sup>·g<sup>-1</sup> in Fig. S5, respectively. And the pore volume of UB-BNC (0.11 cm<sup>3</sup>·g<sup>-1</sup>) is much larger than that of UB-NC (0.03 cm<sup>3</sup>·g<sup>-1</sup>) due to the pore-forming ability of B<sub>2</sub>O<sub>3</sub>. UB-NC and UB-BNC catalysts also show high graphitization by the XRD test in Fig. 6h. And the Raman spectra in Fig. 6i show

that I<sub>D</sub>/I<sub>G</sub> of UB-BNC (1.05) is lower than UB-NC (1.59), indicating that the disorder of UB-BNC catalyst decreases after introduction of B atoms. And the introduction of B atoms into the carbon skeleton is also demonstrated by the presence of B-N and B-C bonds in the FT-IR spectra of UB-BNC (Fig. 6g).

As for the components and active site, the content of N atom in UB-NC catalyst is 13.78 % in Fig. 6j, which is much higher than that of MP-NC and N-doped carbon-based catalysts reported in the literature [45, 46]. After B doping, the content of N atom in UB-BNC catalyst is still 10.65 % and the content of B atom is 3.03 %. In the fitted N1s spectrum (Fig. 6k), only pyridinic-N and graphite-N appear in UB-NC, and the share is 33.07 % and 66.93 % respectively, indicating that the graphite-N may be the primary reason for higher catalytic hydrogenation ability of UB-NC than that of MP-NC. And in UB-BNC after B doping, graphite-N combines with B atoms to form B-N bond of 17.56 %. The corresponding B1s spectrum also proves the B-N bond formation with 48.61 % proportion (in Fig. 6l). Further, EPR in Fig. S6 was performed to test N vacancies. The UB-BNC catalyst shows the symmetrical signal lines centered on  $g = 2.003$  due to unpaired electrons in  $\pi$ -conjugated structures, indicating the presence of unpaired electrons in the N-vacancy and coordination defects in the UB-BNC catalyst. However, from the comparison of UB-NC and UB-BNC, the signal intensity of UB-BNC catalyst is slightly weaker, indicating that fewer unpaired electrons in the defective N-vacancy of UB-BNC catalyst than that of UB-NC catalyst. The result further confirmed that the B doping makes the B-N and graphite-N with more perfect electron pairing have strong effect on the surface of UB-BNC.

The UB-NC and UB-BNC also show alkalinity and acidity from  $\text{CO}_2$ -TPD and  $\text{NH}_3$ -TPD in Figs. 6m and 6n. Therein, N atom acts as Lewis base, and C atom at defect site acts as Lewis acid, exhibiting weak acid-base interaction in UB-NC. With the introduction of B atom, the B atoms replace partial C atoms and act as stronger Lewis acid in UB-BNC to form Lewis acid center and Lewis base center. The synergistic effect of the Lewis acid-base pairs (B-N bond) supports the UB-BNC catalyst to complete 6 cycles of experiments in Fig. 6o. And the catalyst can still maintain stable physi-chemical properties after cyclic experiments (shown in Fig. S7). The pore size and chemical bond of UB-BNC catalyst remain almost unchanged in FT-IR, likewise the  $\text{N}_2$  physical adsorption and desorption curve (Fig. S7a,b). From XPS of Fig. S7c, the N and B atom content (10.50 % and 2.97 %) is similar to the fresh catalyst. The fitted spectra of each element in Fig. S7d,e,f show the content distribution of B-N bond in N1s and B1s was basically consistent with the fresh catalyst, which further proved the stability of UB-BNC catalyst.

The above results show that the crystallinity of 2D-COFs structure has a great influence on the properties of catalyst, hence affect the hydrogenation performance. The results also show that B atom has an outstanding contribution to nitrobenzene catalytic hydrogenation. Depending on the rigid structure of 2D-COFs itself, the doping of heteroatoms makes the carbon skeleton of the catalyst more solid, and the active site more stably embedded in, supporting the operation of catalytic hydrogenation. Compared with MP-BNC catalyst, UB-BNC catalyst has more ordered carbon structure, more N atom content and graphite-N, providing an environment to form more B-N bond as active sites that expose on the surface and pore of UB-BNC, thus enhance the activity of catalyst.

Finally, the further explorations of the catalytic performances of UB-BNC in other nitro compounds hydrogenation were investigated and the results are shown in Table S3. For halogenated nitrobenzene, the hydrogenation properties are various for the different positions of halogenated atoms. The conversion of substrate with the electron-withdrawing groups (-OH, -COOH) can reach greater than 95 %, thanks to the large numbers of N atoms in UB-BNC. For the electron-donating group -NH<sub>2</sub>, the conversion of p-amino-nitrobenzene is relative difficult, while the substrate conversion can also reach greater than 93 % by prolonging the reaction time. For the polycyclic substrate hydrogenation, UB-BNC shows relative weaker catalytic ability, it shows about 90 % substrate conversion by increasing the reaction time.

### 3.4. DFT calculations and reaction mechanism

From above results, it can conclude that hetero-atoms doping is an

effective measure to improve catalytic hydrogenation activity. In order to further nail down the advantages of heteroatoms doping and assess the catalytic mechanism in the catalytic hydrogenation reaction, DFT calculations were carried out by using a  $6 \times 6$  unit of graphene as the theoretical fundamental model [42,47].

#### 3.4.1. The N-doping functions in carbon nanosheets

From the experiment data, the UB-NC catalyst also shows catalytic activity in nitrobenzene hydrogenation, indicating that the C-N bond has ability to activate  $\text{H}_2$  molecules and convert substrate. Thus, the N-doping carbon nanosheets was researched firstly.

According to the second law of thermodynamics, defects in crystalline materials cannot be eliminated, as do the carbon-based materials [47]. Based on the original carbon nanosheet model and defective carbon nanosheet model (Fig. S8), N-doped carbon nanosheet models are constructed by replacing C atoms with N atoms. Among them, different N species are established, including pyridinic-N (Fig. S10b), pyrrolic-N (Fig. S10c) and two types of graphite-N. One of the graphite-N is constructed on the original carbon nanosheet as N-Q (Fig. S10a) and the other is on the defective carbon nanosheet as N-Qd [45,46]. Considering the determination of the optimum doping position, we design three models of N-Qd at different defect positions as N-Qd-1, N-Qd-2 and N-Qd-3 model (Fig. S10d,e,f).

Fig. S9 shows the charges distribution results of the original carbon nanosheet and the defective carbon nanosheet. It can be seen that the charges distribution on each carbon atom on the defective carbon are not even, indicating that the electron migration tends to occur on carbon atoms near defects [48]. It was reported that the doping heteroatoms with different electronegativity can make carbon networks possess the properties of asymmetric charges, spin density redistribution, electronic properties optimization, and active sites generation [49]. In N doped models of Fig. S10, N atoms and adjacent C atoms have more charge aggregation, and more of the carbon atoms are charged than that on defective carbon nanosheets model. It indicates that the doping of N atoms can accelerate the charge transfer on the catalyst more than the defect doping. By comparing different types of N species, it is clear that the negative charge accumulates on the N atom of graphite-N, which is higher than other N doped models. On the defective structures such as pyridinic-N, pyrrolic-N and N-Qd model, besides the charged N atom and the contiguous C atoms, the charged C atoms also appear at the defective position, especially in the N-Qd structure. The charge delivery of N-Q can only appear between the N atom and the adjacent C atoms, but N-Qd can combine the intrinsic defects of carbon nanosheets and the advantages of graphite-N to achieve charge migration of C-N and C-C bonds, so that the adsorption behavior of  $\text{H}_2$  and substrate molecules are enhanced in this strong ability of charge transfer circumstance. The analysis of electron density in Fig. S10 shows that the N-Q, pyridinic-N and pyrrolic-N models have more positrons gathered on the N atom, while that of N-Qd model migrates to the defect position and adjacent C atoms. And the DOS analysis in Fig. S11 indicates that the valence band region and conduct band region are supported mainly by N-p orbital states. The p electron transfer between C atoms and N atoms, and the total DOS pass through Fermi level in N-Qd series models, indicating that the electron from the valence band region can achieve energy level transition to conduct band region. In this way, graphite-N tends to increase the electron transfer rate and cooperate with the defect structure to activate the entire carbon nanosheets and exert catalytic activity.

In addition, the adsorption and dissociation of  $\text{H}_2$  molecule is always accompanied by the reaction process. The adsorption energy ( $E_{ad}$ ) was calculated based on the optimized models. Several possible adsorption sites of  $\text{H}_2$  molecules on the different modes are considered, including the top site, bridge site, and six-membered ring or structure defect [7]. The optimized N doped carbon nanosheets models are shown in Figs. S12-S16. And Tables S4-S6 list the  $E_{ad}$  values of  $\text{H}_2$  on the different individual models, respectively. It shows that the  $E_{ad}$  value in defect site is mostly higher than other adsorption position in majority models,

indicating that  $\text{H}_2$  molecules tend to adsorb on the hollow or defect rings of the carbon nanosheets due to the higher electron density of the defect positions. Likewise, the  $E_{ad}$  value on series of N-Qd models is much higher than N-Q, pyridinic-N and pyrrolic-N models. And the  $E_{ad}$  differs widely when the N atoms are at different positions. The  $E_{ad}$  of N-Qd-1 model is 0.12466 eV, which is higher than other models. It is shown that the N atom at a specific position can better bind the defects to attract  $\text{H}_2$  molecules.

The dissociation process of  $\text{H}_2$  and the corresponding transition state (TS) were also investigated in Fig. 7. We set the energy of the initial adsorption model to zero, facilitates comparison of the reaction energy and barrier of  $\text{H}_2$  dissociation. The results show that the minimum barrier for  $\text{H}_2$  dissociation appears on N-Qd-1 model of 2.23 eV under the same initial conditions. For other models, the high barrier makes it difficult to complete although the final reaction energy is more eximious. As the distance of the H-H bond is elongated, the C-N bond length also have changed from 1.345 Å to 1.538 Å in Fig. S17d, the charge of N atom and C atom are partially transferred to H atoms.

#### 3.4.2. The B/N co-doping in carbon nanosheets and the function of B species

It can be seen that the catalytic activity of the catalyst with B doping is much higher than that of single N-doped carbon nanosheets. Thus, B atoms were also embedded to construct different kinds of B/N co-doped carbon nanosheets to investigate the function of B modification. Similarly, the doping positions of B atoms on N-Qd models are designed and named as 1-B/N-Qd-n, 2-B/N-Qd-n and 3-B/N-Qd-n (n represents 1, 2 and 3, means the different positions of B atom). All B/N-Qd models underwent geometric optimization, as shown in Figs. S18–21. B atoms introduction makes more charges aggregation on B atoms and N atoms. By contrast, the negative charges decrease slightly on N atom in pyridinic-N and N-Q model, while the negative charges increase in pyrrolic-N and N-Qd model, and the B atoms also have more positive charges accordingly. And the electron density analysis shows that the B atom introduction and its position dictates the ability of electron transfer. The electron gathering on C atoms and N atoms in B/N co-doped carbon nanosheets, shows the strong electron-rich property.

The DOS analysis in Fig. S22 shows that the valence band region and conduct band region are supported mainly by N-p orbital states and B-p orbital states. The p electron transfer between B atoms and N atoms leads to the tight bonding of the B-N bond [50]. Combined with XPS analysis, it can be inferred that N-Qd models may have more dominant to

consolidate B atoms and provide more potential active sites than other models. Furthermore, this unique electronic state facilitates the chemisorption and dissociation of  $\text{H}_2$ . The calculation results about the adsorption ability to  $\text{H}_2$  are shown in Figs. S23–34 and Tables S7–11.

Due to the difference in electronegativity, electron will transfer from N atom to B atom inevitably during the process of  $\text{H}_2$  dissociation in Fig. 8 and Fig. S35. After  $\text{H}_2$  dissociation, the H atom adsorbed on the B atom exhibits more electron-rich state, the other one adsorbed on the C atom shows electron-deficient states. At the same time, the position of defect shows the strong electron-rich state. Since the electronegativity of the B atom is less than that of the N atom, the B atom as Lewis acid site is more inclined to form a hydride B-H<sup>+</sup>. The dissociation distance of H-H bond is obviously larger until broken on the model with the B atoms introduction. The results may explain that  $\text{H}_2$  molecules are adsorbed and dissociated easily on the surface of BNC catalyst. From the transition state (TS) analysis, it shows that the values of barrier energies are vary widely with  $\text{H}_2$  dissociation on all sorts of N species and the position of B atom. The lowest barrier energy of  $\text{H}_2$  dissociation is 1.395 eV on 2-B/N-Qd-1 carbon nanosheet. And the whole reaction energy on 2-B/N-Qd-1 model (61.66 KJ/mol) is obviously lower than that on N-Qd-1 model (100.05 KJ/mol) without B doping. As shown in Fig. S36, the B-N bond length (1.852 Å) is longer than that of typical distance of B-N (1.440 Å) [51] during the reaction, and Lewis acid and Lewis base shift away but still remain the interaction in each other when  $\text{H}_2$  is dissociated. B/N co-doped carbon nanosheets, a rigid structure, puts the whole reaction environment in an equilibrium system when  $\text{H}_2$  is adsorbed and dissociated. As a fixed all-solid FLP active center, B-N bond is favorable for  $\text{H}_2$  adsorption and dissociation during the nitrobenzene hydrogenation process, confirming the reactivity of FLP despite harsh reaction conditions are needed. All in all, the DFT calculation results are well consistent with the experimental data, the rationality of N and B co-doping strategy is confirmed and the synergistic effect of these two heteroatoms can promote  $\text{H}_2$  adsorption and dissociation, resulting high efficiency catalytic performance even though no metal species participation in the hydrogenation under  $\text{H}_2$  ambience.

Based on 2-B/N-Qd-1 model, the analysis of different quantity of B-N bond and the coexistence of multiple N-species were added in Fig. S37 and Fig. S38 [52]. From population analysis and electron density of Fig. S37, when three B-N bonds or five B-N bonds coexist, the charge is basically distributed between the B atom and N atom, which hardly influence C atoms. The same change is true of electron density. And the adsorption energy of  $\text{H}_2$  molecule (0.10 eV and 0.12 eV) are obviously

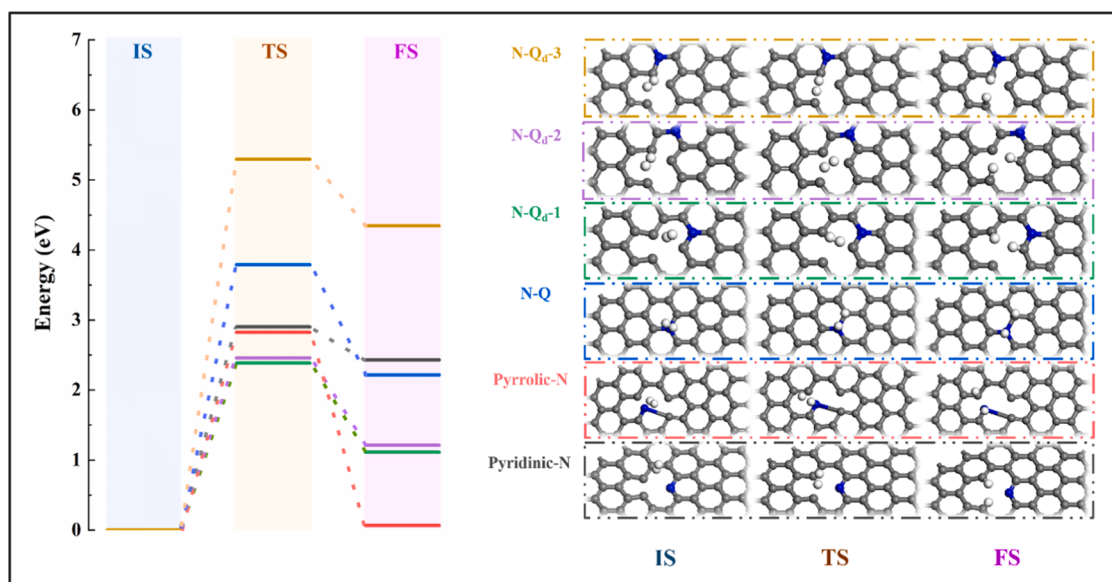


Fig. 7. The reaction energy diagram of  $\text{H}_2$  dissociation on N-doped carbon nanosheets.

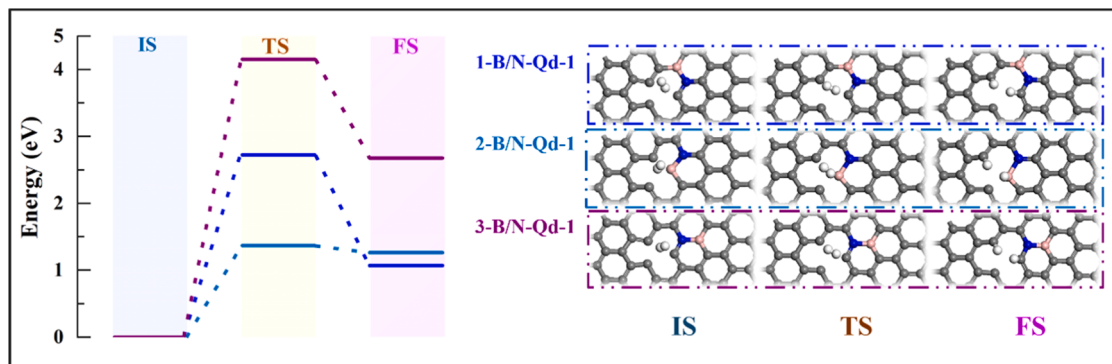


Fig. 8. The reaction energy diagram of  $\text{H}_2$  dissociation on B/N co-doped carbon nanosheets.

weaker than that of 2-B-N-Qd-1 model. Obviously, the B-N bond needs achieve electronic communication with the C atoms to stimulate the activation of the carbon support, rather than only relying on a mass of B-N bond, which indicates the necessary of highly graphitized carbon support in this catalytic system. Similarly, the coexistence of B atom, pyridinic-N and graphite-N drives the charge change more only between the B and N atoms in Fig. S38. And the adsorption capacity of  $\text{H}_2$  (0.10 eV) is also weaker than that of 2-B-N-Qd-1 model, which more intuitively reflects that the combination of defective graphite-N and B atoms can promote the activation of  $\text{H}_2$  molecules.

### 3.4.3. Reaction mechanism proposal

The reaction route of nitrobenzene hydrogenation to aniline is shown in Fig. 9. As reported, nitrobenzene hydrogenation process has two pathways, direct pathway and indirect pathway. The direct pathway is

that the nitrobenzene is reduced to nitrosobenzene and N-phenyl-hydroxylamine, and finally to aniline with gradually hydrogenation and dehydration. The indirect pathway is accompanied by the formation of intermediates and by-product (azoxybenzene, azobenzene, hydrazobenzene) due to the condensation of nitrosobenzene and N-phenyl-hydroxylamine and continuous hydrogenation. The two different pathways are shown in Fig. S39. By referring to the literature [7], we design the experiment that azobenzene was hydrogenated at 180 °C and 4 Mpa  $\text{H}_2$  pressure for 6 h using MP-BNC and UB-BNC as catalyst severally. The experiment results show that no aniline was produced, indicating that the hydrogenation process catalyzed by BNC follows the direct pathway.

Based on the above results, the possible catalytic pathways were proposed for the reaction catalyzed by NC and BNC catalysts, respectively. In the nitrobenzene hydrogenation process, the adsorption and

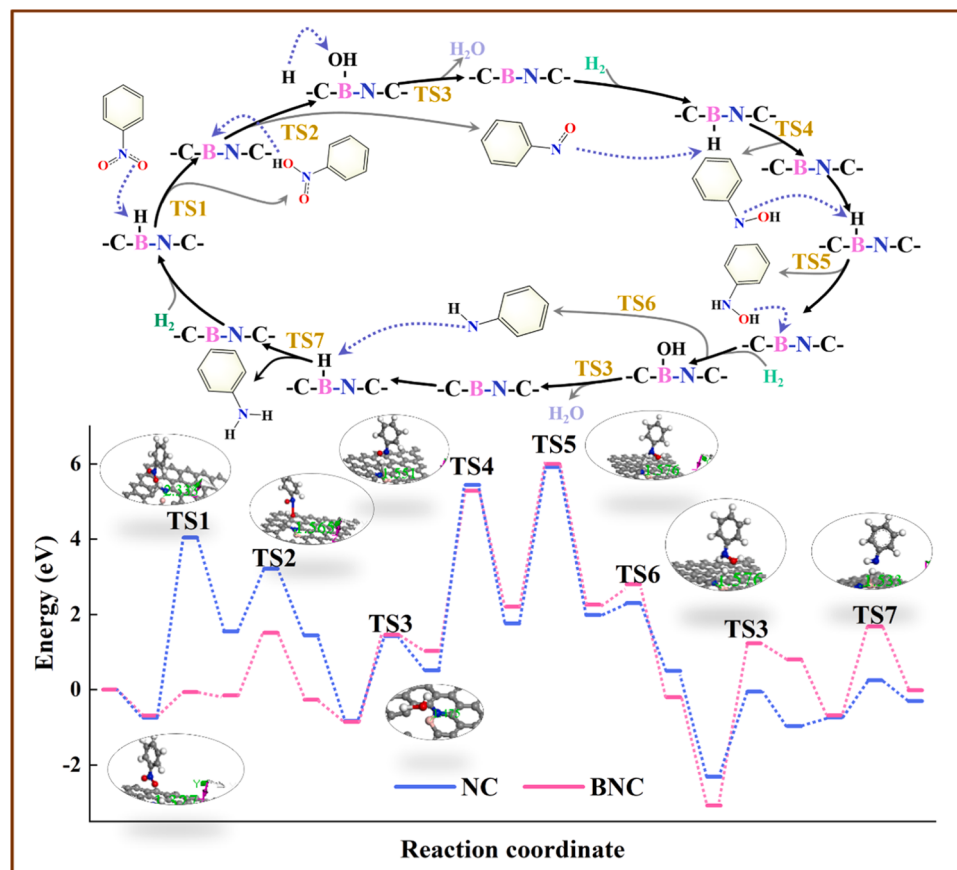


Fig. 9. The reaction pathway and energy profiles for nitrobenzene hydrogenation to aniline over NC and BNC catalysts.

dissociation of  $H_2$  occurs three times. Two  $H$  protons after the first dissociation sustainably attack one  $O$  atom of nitrobenzene, until the  $H_2O$  molecule formed along with the production of nitrosobenzene. In this process, the distance of the B-N bond was continuously pulled from the initial distance of 1.327–2.333 Å, and finally returned to the stable distance 1.555 Å. This proves that not only the carbon material is a rigid structure, but also the prepared BNC catalyst conforms to the design concept of all-solid-state FLP catalyst. With the second dissociation process of  $H_2$ ,  $H^*$  begins to attract another  $O$  atom to form -OH group, and the other  $H^*$  adsorbs on N atom. The electron-rich N atom makes this step harder, which make the TS5 show the highest barrier in the whole process. After the final  $H_2$  dissociation,  $H^*$  first attacks -OH to form  $H_2O$ . And the other  $H^*$  completes the final hydrogenation to obtain the final product of aniline. In Fig. 9, the adsorption capacity of aniline on BNC catalyst is weaker and easier to desorb. In the process of nitrobenzene hydrogenation, the B-N distance of UB-BNC catalyst was constantly changing, from initial state of 1.44–2.333 Å, and then back to the initial state. And the whole carbon material did not change during the reaction process, indicating that the catalyst had a rigid carbon structure, and the change of B-N bond also directly proves that the UB-BNC catalyst presents FLP reactivity.

#### 4. Conclusions

In summary, cost-effective all-solid FLP metal-free B/N co-doped carbon nanosheets is developed by pyrolysis of 2D-COFs and post-doping of B atoms. The B/N co-doped carbon nanosheet exhibits excellent catalytic performance and stability in hydrogenation reaction under  $H_2$  ambience. Among them, UB-BNC metal-free catalyst exhibits the best catalytic performance with 100 % conversion of nitrobenzene and 99.89 % selectivity to aniline. The characterization analyses indicate that introduction of B atoms can enhance the strength and amount of the acid and base sites, and make the carbon nanosheets orderly. The introduction of B atoms promotes the formation of B-N bond as a fixed all-solid FLP active center, which is an extremely probably active center for hydrogenation reaction to enhance  $H_2$  adsorption and dissociation. DFT calculations show that the defects and B atoms doping efficiently accelerate the charges aggregation between B-N bonds to form Lewis pairs, and the TS searching calculations shows the significant decrease of  $H_2$  dissociation barrier energy and the reaction energy on the catalysts from B/N co-doped defective carbon nanosheets model. The results in this work can demonstrate the effectiveness of N and B co-doping strategy, and the obtained all-solid FLP metal-free active center results in high efficiency catalytic performance even though no metal species participation in the nitrobenzene hydrogenation under  $H_2$  system. This work provides a good strategy for the future research of all-solid FLP metal-free catalyst in the catalytic hydrogenation.

#### CRediT authorship contribution statement

**Yang Liu:** Writing – original draft, Formal analysis, Investigation, Visualization, Data curation, Writing – review & editing. **Dong Han:** Investigation, Visualization, Methodology. **Fang Hao:** Data curation, Supervision, Software. **Wei Xiong:** Formal analysis, Methodology, Supervision, review & editing, Supervision. **Pingle Liu:** Supervision, Validation, Visualization.

#### Declaration of Competing Interest

The authors declare that they have no known competing financial interests or personal relationships that could have appeared to influence the work reported in this paper.

#### Data availability

Data will be made available on request.

#### Acknowledgements

This work is supported by NSFC (21908185, 22078277), Hunan Provincial Natural Science Foundation of China (2021JJ30658, 2021JJ30663), The Science and Technology Innovation Program of Hunan Province (2022RC1117), Collaborative Innovation Center of New Chemical Technologies for Environmental Benignity and Efficient Resource Utilization, and Environment-friendly Chemical Process Integration Technology Hunan Province Key laboratory.

#### Appendix A. Supporting information

Supplementary information includes several characterization results include partial XRD spectra, SEM pictures,  $N_2$  adsorption-desorption isotherms, and the established calculation models. Supplementary data associated with this article can be found in the online version at doi:10.1016/j.apcatb.2023.123338.

#### References

- [1] S. Liu, Y. Li, X. Yu, S. Han, Y. Zhou, Y. Yang, H. Zhang, Z. Jiang, C. Zhu, W.X. Li, C. Wöll, Y. Wang, W. Shen, Tuning crystal-phase of bimetallic single-nanoparticle for catalytic hydrogenation, *Nat. Commun.* 13 (2022) 1–10, <https://doi.org/10.1038/s41467-022-32274-4>.
- [2] J. Kou, W.D. Wang, J. Fang, F. Li, H. Zhao, J. Li, H. Zhu, B. Li, Z. Dong, Precisely controlled Pd nanoclusters confined in porous organic cages for size-dependent catalytic hydrogenation, *Appl. Catal. B Environ.* 315 (2022), 121487, <https://doi.org/10.1016/j.apcatb.2022.121487>.
- [3] X. Zhang, Y. Zhou, G. Li, L. Zhang, C. Yin, Y. Yang, H. Wang, F. Feng, L. Wei, Q. Zhang, F. Yang, L. Lin, C. Lu, X. Li, A highly sulfur resistant and stable heterogeneous catalyst for liquid-phase hydrogenation, *Appl. Catal. B Environ.* 315 (2022), 121566, <https://doi.org/10.1016/j.apcatb.2022.121566>.
- [4] H. Yang, Y. Dang, X. Cui, X. Bu, J. Li, S. Li, Y. Sun, P. Gao, Selective synthesis of olefins via  $CO_2$  hydrogenation over transition-metal-doped iron-based catalysts, *Appl. Catal. B Environ.* 321 (2023), 122050, <https://doi.org/10.1016/j.apcatb.2022.122050>.
- [5] B.B. Wang, B. Gao, X.X. Zhong, R.W. Shao, K. Zheng, Structure and photoluminescence of boron and nitrogen co-doped carbon nanorods, *Mater. Sci. Eng. B Solid-State Mater. Adv. Technol.* 209 (2016) 60–65, <https://doi.org/10.1016/j.mseb.2016.03.008>.
- [6] J. Xi, Q. Wang, J. Liu, L. Huan, Z. He, Y. Qiu, J. Zhang, C. Tang, J. Xiao, S. Wang, N, P-dual-doped multilayer graphene as an efficient carbocatalyst for nitroarene reduction: a mechanistic study of metal-free catalysis, *J. Catal.* 359 (2018) 233–241, <https://doi.org/10.1016/j.jcat.2018.01.003>.
- [7] W. Xiong, Z. Wang, S. He, F. Hao, Y. Yang, Y. Lv, W. Zhang, P. Liu, H. Luo, Nitrogen-doped carbon nanotubes as a highly active metal-free catalyst for nitrobenzene hydrogenation, *Appl. Catal. B Environ.* 260 (2020), 118105, <https://doi.org/10.1016/j.apcatb.2019.118105>.
- [8] J. Wu, C. Wen, X. Zou, J. Jimenez, J. Sun, Y. Xia, M.T. Fonseca Rodrigues, S. Vinod, J. Zhong, N. Chopra, I.N. Odeh, G. Ding, J. Lauterbach, P.M. Ajayan, Carbon dioxide hydrogenation over a metal-free carbon-based catalyst, *ACS Catal.* 7 (2017) 4497–4503, <https://doi.org/10.1021/acscatal.7b00729>.
- [9] Y. Wen, C. Huang, L. Wang, D. Hulicova-Jurcakova, Heteroatom-doped graphene for electrochemical energy storage, *Chin. Sci. Bull.* 59 (2014) 2102–2121, <https://doi.org/10.1007/s11434-014-0266-x>.
- [10] H. Zhang, C. Zhang, Y. Zhang, P. Cui, Y. Zhang, L. Wang, H. Wang, Y. Gao, P/N co-doped carbon derived from cellulose: a metal-free photothermal catalyst for transfer hydrogenation of nitroarenes, *Appl. Surf. Sci.* 487 (2019) 616–624, <https://doi.org/10.1016/j.apsusc.2019.05.144>.
- [11] D. Yan, J. Li, M. Zahid, J. Li, Y. Zhu, Efficient catalytic selective hydrogenation of furfural to furfuryl alcohol over Pt-supported on surface amino functionalized hexagonal BN nanosheets, *Appl. Surf. Sci.* 609 (2023), 155308, <https://doi.org/10.1016/j.apsusc.2022.155308>.
- [12] C. Saka, Phosphorus decorated g-C<sub>3</sub>N<sub>4</sub>-TiO<sub>2</sub> particles as efficient metal-free catalysts for hydrogen release by NaBH<sub>4</sub> methanolysis, *Fuel* 322 (2022), 124196, <https://doi.org/10.1016/j.fuel.2022.124196>.
- [13] L. Li, L. Li, C. Cui, H. Fan, R. Wang, Heteroatom-doped carbon spheres from hierarchical hollow covalent organic framework precursors for metal-free catalysis, *ChemSusChem* 10 (2017) 4921–4926, <https://doi.org/10.1002/cssc.201700979>.
- [14] D.J. Nash, D.T. Restrepo, N.S. Parra, K.E. Giesler, R.A. Penabade, M. Aminpour, D. Le, Z. Li, O.K. Farha, J.K. Harper, T.S. Rahman, R.G. Blair, Heterogeneous metal-free hydrogenation over defect-laden hexagonal boron nitride, *ACS Omega* 1 (2016) 1343–1354, <https://doi.org/10.1021/acsomega.6b00315>.
- [15] W. Meng, X. Feng, H. Du, Frustrated Lewis pairs catalyzed asymmetric metal-free hydrogenations and hydrosilylations, *Acc. Chem. Res.* 51 (2018) 191–201, <https://doi.org/10.1021/acs.accounts.7b00530>.
- [16] Q. Shen, X. Li, R. Li, Y. Wu, Application of metal-organic framework materials and derived porous carbon materials in catalytic hydrogenation, *ACS Sustain. Chem. Eng.* 8 (2020), <https://doi.org/10.1021/acssuschemeng.0c06849>.

[17] X. Chen, Q. Shen, Z. Li, W. Wan, J. Chen, J. Zhang, Metal-free H<sub>2</sub> activation for highly selective hydrogenation of nitroaromatics using phosphorus-doped carbon nanotubes, *ACS Appl. Mater. Interfaces* 12 (2020) 654–666, <https://doi.org/10.1021/acsmi.9b17582>.

[18] P.A. Chase, G.C. Welch, T. Jurca, D.W. Stephan, Metal-free catalytic hydrogenation, *Angew. Chem. Int. Ed.* 46 (2007) 8050–8053, <https://doi.org/10.1002/anie.200702908>.

[19] X.Y. Sun, B. Li, T.F. Liu, J. Song, D.S. Su, Designing graphene as a new frustrated Lewis pair catalyst for hydrogen activation by co-doping, *Phys. Chem. Chem. Phys.* 18 (2016) 11120–11124, <https://doi.org/10.1039/c5cp07969a>.

[20] D. Deng, K.S. Novoselov, Q. Fu, N. Zheng, Z. Tian, X. Bao, Catalysis with two-dimensional materials and their heterostructures, *Nat. Nanotechnol.* 11 (2016) 218–230, <https://doi.org/10.1038/nnano.2015.340>.

[21] A. Cardil, S. Monedero, G. Schag, M. Tapia, Jo u rn a ro of, *J. Alloy. Compd.* (2021) 165187, <https://doi.org/10.1016/j.jpcatb.2022.122017>.

[22] T.C. Johnstone, G.N.J.H. Wee, D.W. Stephan, Accessing frustrated Lewis pair chemistry from a spectroscopically stable and classical Lewis acid-base adduct, *Angew. Chem. Int. Ed.* 57 (2018) 5881–5884, <https://doi.org/10.1002/anie.201802385>.

[23] A. Palazzolo, S. Carencio, Phosphines Modulating the catalytic silane activation on nickel-cobalt nanoparticles, tentatively attributed to frustrated Lewis pairs in a colloidal solution, *Chem. Mater.* 33 (2021) 7914–7922, <https://doi.org/10.1021/acs.chemmater.1c03105>.

[24] W. Zhang, Z. Yang, H. Wang, L. Lu, D. Liu, T. Li, S. Yan, H. Qin, T. Yu, Z. Zou, Crystal facet-dependent frustrated Lewis pairs on dual-metal hydroxide for photocatalytic CO<sub>2</sub> reduction, *Appl. Catal. B Environ.* 300 (2022), 120748, <https://doi.org/10.1016/j.apcatb.2021.120748>.

[25] Y. Ding, X. Huang, X. Yi, Y. Qiao, X. Sun, A. Zheng, D.S. Su, A heterogeneous metal-free catalyst for hydrogenation: Lewis acid-base pairs integrated into a carbon lattice, *Angew. Chem. Int. Ed.* 57 (2018) 13800–13804, <https://doi.org/10.1002/anie.201803977>.

[26] Z. Chen, X. Li, C. Yang, K. Cheng, T. Tan, Y. Lv, Y. Liu, Hybrid porous crystalline materials from metal organic frameworks and covalent organic frameworks, *Adv. Sci.* 8 (2021) 1–27, <https://doi.org/10.1002/advs.202101883>.

[27] Z. Wang, S. Zhang, Y. Chen, Z. Zhang, S. Ma, Covalent organic frameworks for separation applications, *Chem. Soc. Rev.* 49 (2020) 708–735, <https://doi.org/10.1039/c9cs00827f>.

[28] N. Keller, T. Bein, Optoelectronic processes in covalent organic frameworks, *Chem. Soc. Rev.* 50 (2021) 1813–1845, <https://doi.org/10.1039/d0cs00793e>.

[29] X. Huang, Z. Wu, H. Zheng, W. Dong, G. Wang, A sustainable method toward melamine-based conjugated polymer semiconductors for efficient photocatalytic hydrogen production under visible light, *Green Chem.* 20 (2018) 664–670, <https://doi.org/10.1039/c7gc02231j>.

[30] J. Liu, S. Yang, F. Li, L. Dong, J. Liu, X. Wang, Q. Pu, Highly fluorescent polymeric nanoparticles based on melamine for facile detection of TNT in soil, *J. Mater. Chem. A* 3 (2015) 10069–10076, <https://doi.org/10.1039/c5ta00185d>.

[31] B.H. Kim, K.S. Yang, Enhanced electrical capacitance of porous carbon nanofibers derived from polyacrylonitrile and boron trioxide, *Electrochim. Acta* 88 (2013) 597–603, <https://doi.org/10.1016/j.electacta.2012.10.123>.

[32] J.A. Baeza, L. Calvo, N. Alonso-Morales, F. Heras, S. Eser, J.J. Rodriguez, M. A. Gilarranz, Effect of structural ordering of the carbon support on the behavior of Pd catalysts in aqueous-phase hydrodechlorination, *Chem. Eng. Sci.* 176 (2018) 400–408, <https://doi.org/10.1016/j.ces.2017.11.015>.

[33] M.S. Dresselhaus, A. Jorio, M. Hofmann, G. Dresselhaus, R. Saito, Perspectives on carbon nanotubes and graphene Raman spectroscopy, *Nano Lett.* 10 (2010) 751–758, <https://doi.org/10.1021/nl904286r>.

[34] J. Wu, P. Wang, F. Wang, Y. Fang, Investigation of the microstructures of graphene quantum dots (GQDs) by surface-enhanced raman spectroscopy, *Nanomaterials* 8 (2018), <https://doi.org/10.3390/nano8100864>.

[35] J. Jin, F. Pan, L. Jiang, X. Fu, A. Liang, Z. Wei, J. Zhang, G. Sun, Catalyst-free synthesis of crumpled boron and nitrogen co-doped graphite layers with tunable bond structure for oxygen reduction reaction, *ACS Nano* 8 (2014) 3313–3321, <https://doi.org/10.1021/nn404927n>.

[36] N. Al-Ansi, A. Salah, J. Lin, G.D. Yang, H.Z. Sun, L. Zhao, Fabrication and synergistic control of ternary TiO<sub>2</sub>/MoO<sub>3</sub>@NC hollow spheres for high-performance lithium/sodium-ion batteries anodes, *Appl. Energy* 334 (2023), 120691, <https://doi.org/10.1016/j.apenergy.2023.120691>.

[37] X. Chen, P. Ye, H. Wang, H. Huang, Y. Zhong, Y. Hu, Discriminating active B-N sites in colloidal B, N dual-doped carbon nano-bundles for boosted Zn-ion storage capability, *Adv. Funct. Mater.* 2212915 (2023) 1–10, <https://doi.org/10.1002/adfm.202212915>.

[38] M. Fan, Q. Yuan, Y. Zhao, Z. Wang, A. Wang, Y. Liu, K. Sun, J. Wu, L. Wang, J. Jiang, A facile “double-catalysts” approach to directionally fabricate pyridinic N-B-pair-doped crystal graphene nanoribbons/amorphous carbon hybrid electrocatalysts for efficient oxygen reduction reaction, *Adv. Mater.* 34 (2022) 1–11, <https://doi.org/10.1002/adma.202107040>.

[39] H. Shang, Z. Jiang, D. Zhou, J. Pei, Y. Wang, J. Dong, X. Zheng, J. Zhang, W. Chen, Engineering a metal-organic framework derived Mn-N<sub>4</sub>-C: XSyatomic interface for highly efficient oxygen reduction reaction, *Chem. Sci.* 11 (2020) 5994–5999, <https://doi.org/10.1039/d0sc02343d>.

[40] A. Pogoreltsev, Y. Tulchinsky, N. Fridman, M. Gandelman, Nitrogen Lewis acids, *J. Am. Chem. Soc.* 139 (2017) 4062–4067, <https://doi.org/10.1021/jacs.6b12360>.

[41] P. Sun, J. Huang, F. Xu, J. Xu, T. Lin, W. Zhao, W. Dong, F. Huang, Boron-induced nitrogen fixation in 3D carbon materials for supercapacitors, *ACS Appl. Mater. Interfaces* 12 (2020) 28075–28082, <https://doi.org/10.1021/acsami.0c02535>.

[42] T. Schiros, D. Nordlund, L. Palova, L. Zhao, M. Levendorf, C. Jaye, D. Reichman, J. Park, M. Hybertsen, A. Pasupathy, Atomistic interrogation of B-N co-dopant structures and their electronic effects in graphene, *ACS Nano* 10 (2016) 6574–6584, <https://doi.org/10.1021/acsnano.6b01318>.

[43] Y. Cao, H. Yu, J. Tan, F. Peng, H. Wang, J. Li, W. Zheng, N.B. Wong, Nitrogen-, phosphorous- and boron-doped carbon nanotubes as catalysts for the aerobic oxidation of cyclohexane, *Carbon* 57 (2013) 433–442, <https://doi.org/10.1016/j.carbon.2013.02.016>.

[44] K. Lin, H. Fang, A. Gao, H. Yu, L. Wang, Q. Yu, L. Gu, Q. Zhang, J. Li, W. Jiang, Nanobull graphites, *Adv. Mater.* 33 (2021) 1–10, <https://doi.org/10.1002/adma.202007513>.

[45] Y. Ma, X. Meng, K. Li, L. Zhang, Y. Du, X. Cai, J. Qiu, Scrutinizing synergy and active site of nitrogen and selenium dual-doped porous carbon for efficient triiodide reduction, *ACS Catal.* 13 (2023) 1290–1298, <https://doi.org/10.1021/ascatal.2c05024>.

[46] J. Cheng, C. Lyu, H. Li, J. Wu, Y. Hu, B. Han, K. Wu, M. Hojaberdi, D. Geng, Steering the oxygen reduction reaction pathways of N-carbon hollow spheres by heteroatom doping, *Appl. Catal. B Environ.* 327 (2023), 122470, <https://doi.org/10.1016/j.apcatb.2023.122470>.

[47] D. Xue, H. Xia, W. Yan, J. Zhang, S. Mu, Defect engineering on carbon-based catalysts for electrocatalytic CO<sub>2</sub> reduction, *Nano Micro Lett.* 13 (1) (2021) 23, <https://doi.org/10.1007/s40820-020-00538-7>.

[48] D. Shi, B. Chang, Z. Ai, H. Jiang, F. Chen, Y. Shao, J. Shen, Y. Wu, X. Hao, Boron carbonitride with tunable B/N Lewis acid/base sites for enhanced electrocatalytic overall water splitting, *Nanoscale* 13 (2021) 2849–2854, <https://doi.org/10.1039/d0nr06857h>.

[49] X. Ma, J. Du, H. Sun, F. Ye, X. Wang, P. Xu, C. Hu, L. Zhang, D. Liu, Boron, nitrogen co-doped carbon with abundant mesopores for efficient CO<sub>2</sub> electroreduction, *Appl. Catal. B Environ.* 298 (2021), 120543, <https://doi.org/10.1016/j.apcatb.2021.120543>.

[50] G. Wang, K. Zheng, Y. Huang, J. Yu, H. Wu, X. Chen, L.Q. Tao, An investigation of the positive effects of doping an Al atom on the adsorption of CO<sub>2</sub> on BN nanosheets: a DFT study, *Phys. Chem. Chem. Phys.* 22 (2020) 9368–9374, <https://doi.org/10.1039/d0cp00714e>.

[51] S. Pang, Z. Wang, X. Yuan, L. Pan, W. Deng, H. Tang, H. Wu, S. Chen, C. Duan, F. Huang, Y. Cao, A facile synthesized polymer featuring B-N covalent bond and small singlet-triplet gap for high-performance organic solar cells, *Angew. Chem. Int. Ed.* 60 (2021) 8813–8817, <https://doi.org/10.1002/anie.202016265>.

[52] W. Lin, H. Chen, G. Lin, S. Yao, Z. Zhang, J. Qi, M. Jing, W. Song, J. Li, X. Liu, J. Fu, S. Dai, Creating frustrated Lewis pairs in defective boron carbon nitride for electrocatalytic nitrogen reduction to ammonia, *Angew. Chem. Int. Ed.* 61 (2022), <https://doi.org/10.1002/anie.202207807>.